

Magnetic field geometry and magnetospheric environment of the strongly magnetic Of?p star NGC 1624-2

S. P. Järvinen¹,[★] S. Hubrig,¹ M. Schöller,² M. Küker,¹ I. Ilyin¹ and S. D. Chojnowski³

¹Leibniz-Institut für Astrophysik Potsdam (AIP), An der Sternwarte 16, D-14482 Potsdam, Germany

²European Southern Observatory, Karl-Schwarzschild-Str 2, D-85748 Garching, Germany

³Apache Point Observatory and New Mexico State University, P.O. Box 59, Sunspot, NM 88349-0059, USA

Accepted 2020 December 16. Received 2020 December 5; in original form 2020 July 28

ABSTRACT

NGC 1624-2 is an O7f?p star with a reported probable polar magnetic field strength ≥ 20 kG, which is the strongest magnetic field ever measured in an O-type star. We study the variability of the mean longitudinal magnetic field $\langle B_z \rangle$ and the mean field modulus $\langle B \rangle$ to obtain constraints on its field geometry. Only one magnetic pole is observable over the rotation cycle. The approximately sinusoidal variation of $\langle B_z \rangle$ and the ratio of the values of the extrema of $\langle B \rangle$ indicate that there is an important component of the field that is dipolar. The $\langle B_z \rangle$ values measured over the rotation cycle are in the range from -0.2 to 4.5 kG, whereas the values for $\langle B \rangle$ vary between 9 and 12 kG. The $\langle B_z \rangle$ values obtained using the O III $\lambda 7455$ emission line are in the range from 0.4 to 2.3 kG and show a variability pattern similar to that detected for the absorption lines. The fact that the phase of the $\langle B_z \rangle$ minimum coincides with the phase of the $\langle B \rangle$ maximum, indicates that the field structure must significantly depart from a centred dipole. Further, we discuss the nature of the observed variable Stokes V profiles corresponding to a longitudinal field of negative polarity detected in the emission He I lines and present the first magnetohydrodynamical numerical simulations of the gas flow in the magnetosphere of this star.

Key words: MHD – polarization – stars: early-type – stars: individual: NGC 1624-2 – stars: magnetic field – stars: winds, outflows.

1 INTRODUCTION

Recent observations indicate that probably only a small fraction of about 7 ± 3 per cent of O-type stars with masses exceeding $18 M_\odot$ (Grunhut et al. 2017) and about 6 ± 3 per cent of early B- and O-type stars (Schöller et al. 2017) have measurable, mostly dipolar magnetic fields. Among the polarimetrically studied O-type stars, all five Galactic stars with Of?p classification possess measurable magnetic fields. These stars exhibit recurrent, and apparently periodic, spectral variations in Balmer, He I, C III, and Si III lines, sharp emission or PCygni profiles in He I and the Balmer lines, and a strong C III blend in emission around 4650 \AA (Walborn 1972). The presence of variable emission in the C III blend and in H α in Of?p stars is indicative of circumstellar structure, related to their magnetospheres. Previous measurements of the mean longitudinal magnetic field for the O7f?p star NGC 1624-2 carried out with ESPaDOs (Echelle SpectroPolarimetric Device for the Observation of Stars) at the Canada–France–Hawaii Telescope between 2012 February 1 and 9 indicated $\langle B_z \rangle = 5.35 \pm 0.5$ kG with a polar magnetic field strength of about 20 kG, which is the strongest magnetic field ever measured in an O-type star (Wade et al. 2012b). All the other Of?p stars with studied magnetic field geometries have $B_{\text{pole}} \leq 2.6$ kG (David-Uraz et al. 2019). The existence of a giant wind-fed dynamical magnetosphere around NGC 1624-2 was discussed by Petit et al.

(2015). A very recent study by Kurtz et al. (2020) reported the detection of coherent pulsation modes in NGC 1624-2 based on Transiting Exoplanet Survey Satellite (TESS; Ricker et al. 2014) high-cadence photometry.

The study of spectral variability using archival optical spectroscopic observations indicated $v \sin i \leq 3 \text{ km s}^{-1}$ and a rotation period of 157.99 ± 0.94 d (Wade et al. 2012b). Due to the presence of the strong magnetic field, slow rotation, and the low projected rotational velocity, a few spectral lines showed magnetic splitting into Zeeman components corresponding to a maximum mean magnetic field modulus of about $\langle B \rangle = 14 \pm 1$ kG. Furthermore, Wade et al. (2012b) reported the detection of reversed Stokes V profiles associated with weak, high-excitation emission O III lines, and suggested that they may form in the low-velocity plasma confined in closed magnetic loops above the stellar surface. They measured a longitudinal field $\langle B_z \rangle = 2.58 \pm 0.7$ kG, which is by more than a factor of 2 smaller than the field measured using photospheric absorption lines. On the other hand, the emission lines He I 5876, 6678, and 7065 exhibited Stokes V profiles with signs consistent with those of the photospheric absorption lines, but yielding a negative mean longitudinal magnetic field. Unfortunately, no field measurements using these lines were presented in the work of Wade et al. (2012b).

The He I emission lines are marked in the paper of Wade et al. as ‘wind lines’. This expression was already used by Howarth et al. (2007) for H α , where the authors discuss some lines as contaminated by ‘windy’ emission. Several studies of magnetic O-type stars concluded that these lines are not formed in the wind,

* E-mail: sjarvinen@aip.de

but are possibly resulting from confined circumstellar material (e.g. Grunhut et al. 2009). In the context of the magnetically confined wind-shock model, it was suggested that most emission comes from scattering by the cooling disc and very little from the wind (Donati et al. 2002).

The detected remarkable characteristics of NGC 1624-2 make it an excellent laboratory to study the impact of a very strong magnetic field on the behaviour of different elements in the stellar photosphere and circumstellar environment. In this work, we discuss for the first time the magnetic field geometry of NGC 1624-2 based on the variability of the longitudinal magnetic field measured using photospheric lines, the longitudinal field measurements using the emission O III and He I lines, and the variability of the magnetic field modulus over the rotation period. Finally, using the NIRVANA code, we discuss the first magnetohydrodynamical (MHD) numerical simulations carried out to understand the field geometry, mass distribution, and the gas motions in the vicinity of NGC 1624-2.

2 OBSERVATIONS

A few polarimetric observations were obtained at the beginning of 2012 (Wade et al. 2012b) with the ESPaDOnS spectropolarimeter installed at the 3.6 m Canada–France–Hawaii Telescope (CFHT) together with one observation from its twin Narval, installed at the 2 m Bernard Lyot Telescope (BLT) on Pic-du-Midi. Six additional ESPaDOnS observations from 2012 September to 2013 January were presented by Grunhut et al. (2017). Subsequently, 16 ESPaDOnS observations were obtained between 2013 August and 2015 September. They are described in more detail in David-Uraz et al. (2021). All the ESPaDOnS data are publicly available in the CFHT Science Archive¹ and both ESPaDOnS and Narval data can be retrieved from the PolarBase² archive (Petit et al. 2014).

Additionally, one Potsdam Echelle Polarimetric and Spectroscopic Instrument (PEPSI; Strassmeier et al. 2015, 2018) spectrum has been recorded in linear polarized light in 2017 October at the 2×8.4 m Large Binocular Telescope (LBT) on Mt. Graham, Arizona and one unpolarized spectrum was also obtained with the Astrophysical Research Consortium Echelle Spectrograph (ARCES; Wang et al. 2003) on the ARC 3.5 m telescope at the Apache Point Observatory (APO) on 2019 March 1.

The logbook of all available observations is presented in Table 1. The recorded linear polarization PEPSI Stokes Q and U spectra and the ARCES spectrum were however very noisy, hence only the Stokes I spectrum was used for measuring the magnetic field modulus. The resolving power of all archival observations is $\sim 65\,000$, while the spectral resolution of the PEPSI spectrum is 130 000 whereas the ARCES spectrum has a resolution of only 31 500. As most of the spectra have moderate signal-to-noise ratios (S/N) in the Stokes I spectra, mostly in the range of 100–150, some spectra obtained during the same night or, in one case, during subsequent nights have been combined to increase the signal for the Stokes V profiles. However, in cases where the S/N of the spectrum was significantly lower than that of the other spectra obtained during the same night, only the spectra with better S/N were used for the analysis of the mean longitudinal magnetic field. Some spectra with low S/N have been included in the analysis of the line intensity variability or used for the measurements of the mean magnetic field modulus, if the Zeeman splitting was detectable on them. Further,

Table 1. Logbook of the observations. The columns give the telescope and instrument configuration, the heliocentric Julian date (HJD), the exposure time, and the S/N around 6100 Å. HJDs followed by a – or | indicate subsequent spectra that were combined to increase the S/N in Stokes V profiles that were used for the $\langle B_z \rangle$ analysis. The HJD followed by a # indicates the spectrum with the overall lowest S/N, and which was not used in our measurements. HJDs followed by a * indicate noisy spectra that were not combined with other spectra obtained at similar epochs.

Configuration	HJD 2 450000+	Exp. time (s)	S/N
CFHT + ESPaDOnS	55958.719	2400	109
CFHT + ESPaDOnS	55959.719	2400	88
CFHT + ESPaDOnS	55960.717	2400	71
CFHT + ESPaDOnS	55961.717	2400	112
CFHT + ESPaDOnS	55966.725	2400	90
TBL + Narval	56011.330	4800	78
CFHT + ESPaDOnS	56197.950–	5400	146
CFHT + ESPaDOnS	56198.014–	5400	146
CFHT + ESPaDOnS	56200.974	5400	130
CFHT + ESPaDOnS	56201.039	5400	148
CFHT + ESPaDOnS	56270.751–	5400	115
CFHT + ESPaDOnS	56270.816–	5400	138
CFHT + ESPaDOnS	56285.761*	5400	93
CFHT + ESPaDOnS	56285.826	5400	127
CFHT + ESPaDOnS	56285.890	5400	131
CFHT + ESPaDOnS	56293.733–	5400	136
CFHT + ESPaDOnS	56293.798–	5400	138
CFHT + ESPaDOnS	56295.861#	5400	19
CFHT + ESPaDOnS	56532.126	5160	156
CFHT + ESPaDOnS	56534.063	5160	154
CFHT + ESPaDOnS	56534.124	5160	135
CFHT + ESPaDOnS	56549.039–	5160	146
CFHT + ESPaDOnS	56549.102–	5160	141
CFHT + ESPaDOnS	56561.028	5160	150
CFHT + ESPaDOnS	56561.091	5160	123
CFHT + ESPaDOnS	56613.913–	5160	112
CFHT + ESPaDOnS	56614.045–	5160	125
CFHT + ESPaDOnS	56621.039	5160	140
CFHT + ESPaDOnS	56621.102	5160	135
CFHT + ESPaDOnS	56665.828–	5160	123
CFHT + ESPaDOnS	56665.889–	5160	149
CFHT + ESPaDOnS	57289.978*	5160	82
CFHT + ESPaDOnS	57290.041	5160	106
CFHT + ESPaDOnS	57291.059	5160	108
LBT + PEPSI	58042.022	3600	70
ARC + ARCES	58543.653	3600	98

to increase the accuracy of the mean longitudinal magnetic field determination, we applied the least-squares deconvolution technique (LSD) described in detail by Donati et al. (1997). To create line masks for the measurements, we have used the Vienna Atomic Line Database (VALD; e.g. Kupka, Dubernet & VAMDC Collaboration 2011; Ryabchikova et al. 2015), adopting the stellar parameters of NGC 1624-2, $T_{\text{eff}} = 35\,000$ K and $\log g = 4.0$ (Wade et al. 2012b). The mask for the photospheric absorption lines includes spectral lines belonging to the elements He, O, and C and is identical to that presented in table 7 in the work of Wade et al. (2012b), apart from He I $\lambda 7281$, which is heavily distorted by numerous strong telluric lines in most of the spectra. In massive magnetic early B-type stars, He and Si are usually inhomogeneously distributed on the stellar surface, with the He abundance spots located close to the magnetic poles and the Si abundance spots close to the magnetic equator. Thus,

¹<https://www.cadc-ccda.hia-ihp.nrc-cnrc.gc.ca/en/cfht/>

²<http://polarbase.irap.omp.eu/>

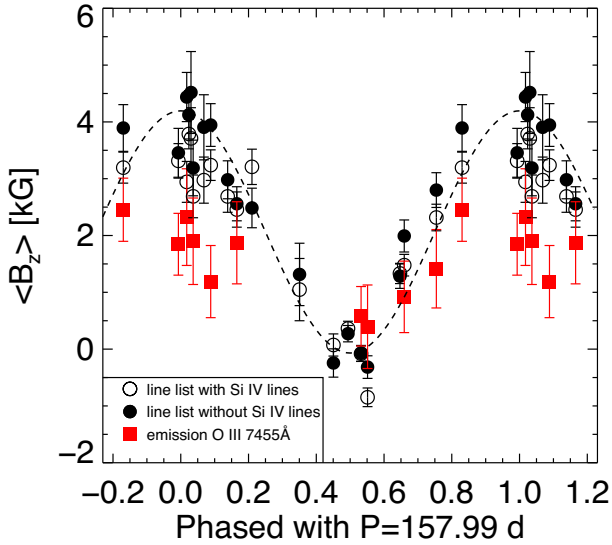


Figure 1. Mean longitudinal magnetic field (B_z) measured using two different line masks and using only the high-excitation line O III $\lambda 7455$ against the rotation phase. The dashed line represents the best sinusoidal least-squares fit solution for the phase curve defined by our magnetic field measurements (see text).

to test a possible inhomogeneous distribution of Si, we also included in our line mask the Si IV lines at $\lambda 4631$ and $\lambda 4654$. The available data set allows us, in addition, for the first time to study the variability of the high-excitation emission O III lines and of the emission wind He I lines over the rotation cycle.

3 MAGNETIC FIELD MEASUREMENTS

3.1 Mean longitudinal magnetic field (B_z)

The mean longitudinal magnetic field is determined by computing the first-order moment of the LSD Stokes V profile according to Mathys (1989):

$$\langle B_z \rangle = -2.14 \times 10^{11} \frac{\int v V(v) dv}{\lambda_0 g_0 c \int [I_c - I(v)] dv}, \quad (1)$$

where v is the velocity shift from the line centre, in km s^{-1} , and λ_0 and g_0 are the normalization values of the line weights. We have adapted for them here the average values of, respectively, the wavelengths (in nm) and the effective Landé factors of all the lines used to compute the LSD profile. The results of our magnetic field measurements using the line mask for the photospheric absorption lines, including the Si lines, the line mask without the Si lines, and the measurements using the high excitation emission line O III $\lambda 7455$ and the strongest emission lines He I $\lambda 5876$ and He I $\lambda 6678$ are presented in Fig. 1 and in Table 2 in Columns 3–7. All LSD profiles for the selected line masks, as well as Stokes I , V , and null profiles for the individual emission lines are shown in Figs A1–A6 in the Appendix. The average effective Landé factors used for the normalization for the line mask including the Si lines and the mask without the Si lines are 1.55 and 1.24, respectively. The corresponding wavelengths are 5013 and 5224 Å. For the profiles calculated using all lines and the line list without the Si lines an integration was made from -120 to $+25 \text{ km s}^{-1}$, for O III $\lambda 7455$ from -70 to $+10 \text{ km s}^{-1}$, for He I $\lambda 5876$ and for He I $\lambda 6678$ from -200 to $+150 \text{ km s}^{-1}$.

In most cases, the false alarm probability (FAP) for the field detections is less than 10^{-6} . According to Donati, Semel & Rees (1992), a Zeeman profile with $\text{FAP} \leq 10^{-5}$ is considered as a definite detection, $10^{-5} < \text{FAP} \leq 10^{-3}$ as a marginal detection, and $\text{FAP} > 10^{-3}$ as a non-detection. Our measurements show that the $\langle B_z \rangle$ values become lower if the Si IV lines are included in the line mask. A possible scenario to explain these measurements would be an inhomogeneous surface element distribution with a region of Si concentration located closer to the magnetic equator. It is also possible that we observe a filling of the lines by emission. Our $\langle B_z \rangle$ measurements in the range from -0.2 to 4.5 kG obtained for the sample of the photospheric absorption lines are in good agreement with the $\langle B_z \rangle$ values reported by Grunhut et al. (2017), but disagree with the measurement of $\langle B_z \rangle = 5.35 \text{ kG}$ reported by Wade et al. (2012b). Assuming a limb-darkening coefficient $u = 0.3$ (Claret & Bloemen 2011) and a centred dipolar magnetic field, we estimate the dipole strength of NGC 1624-2 $B_d \geq 16 \text{ kG}$ according to equation 1 of Preston (1967). The dashed line in Fig. 1 represents the best sinusoidal least-squares fit solution for the phase curve defined by our magnetic field measurements using the line mask for photospheric absorption lines, without the Si IV lines. The rotation phase presented in Table 2 in the second column is calculated using the rotation period of 157.99 d adopted by Wade et al. (2012b) and the initial epoch for the phase origin $\text{HJD}_0 = 2455955.94 \pm 0.21$ corresponding to the maximum of the longitudinal field phase curve. The fitted sinusoid has an amplitude $A_{\langle B_z \rangle} = 2132 \pm 364 \text{ G}$ and a mean value $\langle B_z \rangle = 2063 \pm 328 \text{ G}$, thus $\langle B_z \rangle_{\text{max}} = 4195 \text{ G}$ and $\langle B_z \rangle_{\text{min}} = -69 \text{ G}$.

Knowing the rotation period, we can estimate the equatorial velocity and the inclination of the rotation axis of the star i . Assuming a radius $R = 9.7 R_\odot$ (Petit et al. 2013) and a projected rotation velocity $v \sin i \leq 3 \text{ km s}^{-1}$ (Wade et al. 2012b), we obtain $i \leq 75^\circ$. Using the well-known relations developed by Stibbs (1950) and Preston (1967) for a centred magnetic dipole tilted to the rotation axis by angle β , we estimate an obliquity angle $\beta \geq 15.5^\circ$. However, with $v \sin i = 1 \text{ km s}^{-1}$, we obtain $i = 19^\circ$ and $\beta = 72^\circ$, i.e. nearly a flip of the two axes, showing that the exact geometry of the magnetic field cannot be determined with the still too loose constraint on $v \sin i$. The measured values of the longitudinal magnetic field of NGC 1624-2 with predominantly positive polarity imply that only one magnetic pole is observable over the rotation cycle. The dynamic spectra of emission and photospheric lines show a single-wave variation of their intensity: the intensity of the lines H α , He II $\lambda 6486$, He I $\lambda 5876$ and $\lambda 6678$ are the strongest close to the positive extremum of $\langle B_z \rangle$ whereas the photospheric absorption lines of He I, C IV, Si IV, and the emission O III lines are the strongest close to the rotation phase 0.5. Examples of the variability of different lines are presented in Fig. 2.

3.2 Mean magnetic field modulus (B)

The availability of the variation curve of the mean magnetic field modulus $\langle B \rangle$ allows us to put stronger constraints on the structure of the magnetic field of NGC 1624-2 as compared to any other magnetic O-type star with unsplit lines. Our measurements of $\langle B \rangle$, which is the average over the visible stellar hemisphere of the modulus of the magnetic field vector, weighted by the local line intensity, are presented in Table 3 and Fig. 3. The field modulus was calculated by fitting the magnetically resolved C IV $\lambda 5812$ line with two Gaussian profiles and using the relation given e.g. by Hubrig & Nesvaci (2007). The uncertainties in the presented $\langle B \rangle$ values are due to the accuracy of the measured wavelengths of the blue and red split line components. Our measurements indicating a field intensity between 9 and 12 kG differ from the measurements reported by Wade et al.

Table 2. Longitudinal magnetic field measurements of NGC 1624-2. The dates are as in Table 1, but with the average of the combined dates if observations were co-added. The rotation phases are listed in Column 2, followed by the measurements using the whole sample of photospheric absorption lines and the sample without the Si IV lines. In Columns 5, 6, and 7, we list the measurements using the high-excitation emission O III $\lambda 7455$ line and the wind He I $\lambda 5876$ and He I $\lambda 6678$ lines.

Date	Phase	$\langle B_z \rangle$ (G)				
		ALL	ALL – Si	O III $\lambda 7455$	He I $\lambda 5876$	He I $\lambda 6678$
55958.719	0.018	2944 \pm 360	4438 \pm 433	2324 \pm 851	–2713 \pm 314	–7420 \pm 791
55959.719	0.024	3787 \pm 261	4125 \pm 425		–2538 \pm 294	–6149 \pm 903
55960.717	0.030	3710 \pm 540	4518 \pm 721		–1418 \pm 453	–7050 \pm 1050
55961.717	0.037	2689 \pm 376	3189 \pm 490	1899 \pm 761	–1818 \pm 259	–6838 \pm 800
55966.724	0.068	2975 \pm 406	3905 \pm 573		–2869 \pm 401	–4837 \pm 1066
56011.330	0.351	1048 \pm 548	1315 \pm 549		–820 \pm 1016	–2417 \pm 1813
56197.982	0.532	–80 \pm 137	–74 \pm 139	578 \pm 524	1674 \pm 224	–65 \pm 468
56201.006	0.551	–848 \pm 164	–316 \pm 199	394 \pm 735	182 \pm 336	312 \pm 508
56270.783	0.993	3314 \pm 304	3456 \pm 430	1846 \pm 544	–2550 \pm 235	–4074 \pm 750
56285.858	0.088	3239 \pm 269	3945 \pm 376	1189 \pm 635	–3201 \pm 185	–4074 \pm 523
56293.765	0.138	2688 \pm 279	2981 \pm 334		–2176 \pm 263	–4121 \pm 595
56532.126	0.647	1332 \pm 178	1284 \pm 215		–1792 \pm 504	–1097 \pm 546
56534.093	0.659	1478 \pm 190	1992 \pm 282	920 \pm 629	–2150 \pm 379	–309 \pm 569
56549.070	0.754	2317 \pm 234	2800 \pm 306	1415 \pm 690	–3524 \pm 232	–3669 \pm 540
56561.059	0.830	3195 \pm 273	3893 \pm 411	2454 \pm 556	–3727 \pm 265	–2431 \pm 567
56613.979	0.165	2457 \pm 310	2559 \pm 300	1872 \pm 723	–5120 \pm 488	–5240 \pm 783
56621.070	0.210	3209 \pm 311	2485 \pm 348		–7846 \pm 460	–3324 \pm 628
56665.858	0.493	363 \pm 128	272 \pm 144		–480 \pm 897	15 \pm 697
57290.550	0.447	73 \pm 195	–244 \pm 249		155 \pm 1058	–620 \pm 732

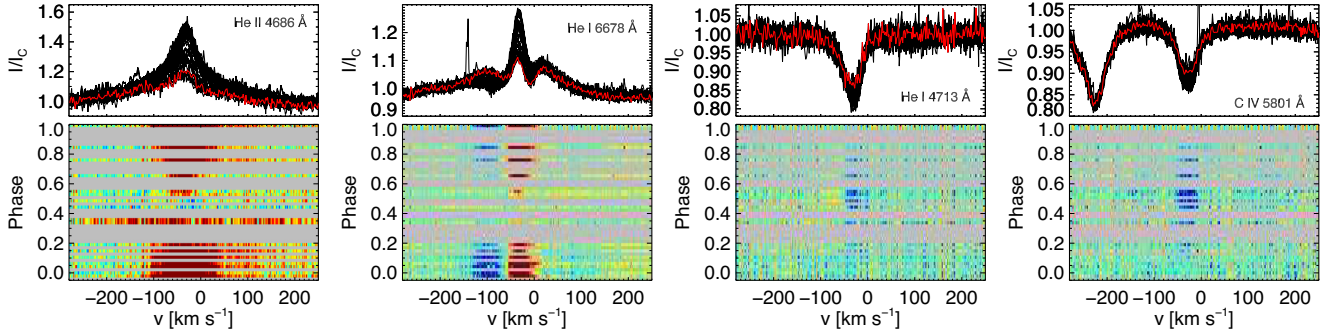


Figure 2. Examples of line intensity variability of the emission lines He II $\lambda 4686$ and He I $\lambda 6678$, and the photospheric absorption lines He I $\lambda 4713$ and C IV $\lambda 5801$ as a function of the rotation phase. In the upper panel, we present all profiles overplotted with the observed weakest profiles highlighted in red colour. The lower panels show the dynamic spectra of the difference between the individual line profiles and the weakest emission or absorption profile.

(2012b), who reported $\langle B \rangle = 15$ kG for the $\lambda 5801$ line and $\langle B \rangle = 13$ kG for the $\lambda 5812$ line using the Narval spectrum. This difference can likely be explained by the Zeeman pattern of the C IV $\lambda 5812$ line. We interpret in our measurements the splitting as a pseudo-doublet, which underestimates the strength of the field modulus.

The approximately sinusoidal variation of $\langle B_z \rangle$ and the ratio of the values of the extrema of $\langle B \rangle$ indicates that there is an important component of the field that is dipolar. Further, a comparison of the variation curves of the mean magnetic field modulus and the mean longitudinal magnetic field shows that the minimum of the mean magnetic field modulus corresponds to the maximum of the mean longitudinal magnetic field. This indicates that the field structure must significantly depart from a centred dipole. It is possible that we see a small shift between the modulus minimum with respect to the positive extremum of the $\langle B_z \rangle$, although the fidelity of such a shift is only barely supported, given the rather large dispersion of the data points. A future confirmation of the presence of a shift is necessary, as this would indicate that the magnetic field structure of NGC 1624-2 slightly departs from a simple dipole.

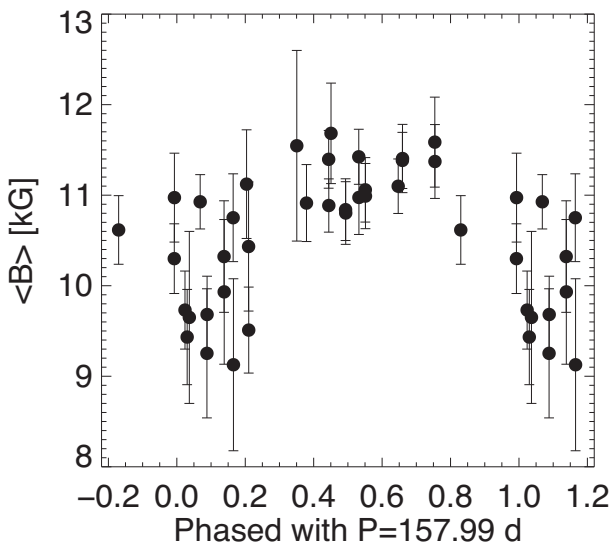
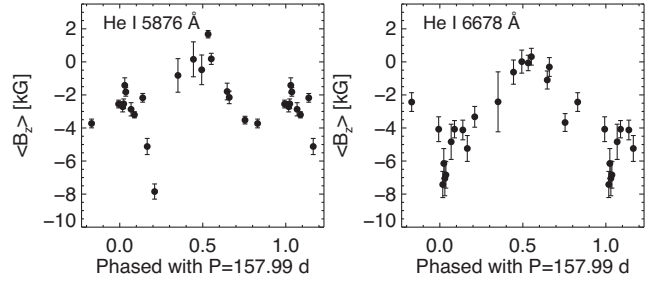
3.3 Emission lines

We confirm the conclusion of Wade et al. (2012b) that the $\langle B_z \rangle$ values measured using the high-excitation O III emission lines, suggested to form in the low-velocity plasma confined in closed magnetic loops above the stellar surface, are significantly lower than those obtained for photospheric absorption lines. The $\langle B_z \rangle$ values obtained using the O III $\lambda 7455$ line are in the range from 0.4 to 2.3 kG and show a variability pattern similar to that detected for the absorption lines.

Interestingly, we detect in the spectra the forbidden [O I] 6300 and 6363 lines, indicating the presence of low-density atomic material in the vicinity of NGC 1624-2. The formation mechanism of these lines is unclear. It was suggested that they originate from disc winds or regions where stellar UV radiation impinges on the disc surface in pre-main-sequence Herbig Ae/Be stars (e.g. Finkenzeller 1985; Corcoran & Ray 1997). It is also possible that the forbidden [O I] 6300 and 6363 lines are formed in magnetospheric accretion columns (Muzerolle et al. 2004). The variability of the strength of these lines is presented in Fig. B1. They are the strongest at the rotational phases

Table 3. The mean magnetic field modulus $\langle B \rangle$ values obtained in the spectra with measurable splitting in the C IV $\lambda 5812$ line.

Date	Phase	$\langle B \rangle$ (G)
55959.719	0.024	9731 \pm 431
55960.717	0.030	9433 \pm 526
55961.717	0.037	9650 \pm 950
55966.725	0.068	10927 \pm 300
56011.330	0.351	11 546 \pm 1053
56197.950	0.532	11 424 \pm 304
56198.014	0.532	10975 \pm 409
56200.974	0.551	11 059 \pm 356
56201.039	0.551	10990 \pm 360
56270.751	0.993	10 299 \pm 385
56270.816	0.993	10 973 \pm 491
56285.826	0.088	9253 \pm 713
56285.890	0.088	9682 \pm 423
56293.733	0.138	10 322 \pm 616
56293.798	0.138	9932 \pm 799
56532.126	0.647	11 099 \pm 301
56534.063	0.659	11 384 \pm 310
56534.124	0.660	11 405 \pm 377
56549.039	0.754	11 586 \pm 497
56549.102	0.754	11 372 \pm 408
56561.028	0.830	10 616 \pm 379
56613.913	0.165	10 751 \pm 485
56614.045	0.165	9127 \pm 950
56621.039	0.210	10 433 \pm 713
56621.102	0.210	9510 \pm 475
56665.828	0.493	10 840 \pm 341
56665.889	0.494	10 803 \pm 346
57289.978	0.444	11 396 \pm 319
57290.041	0.444	10 886 \pm 294
57291.059	0.451	11 683 \pm 555
58042.022	0.204	11 122 \pm 600
58543.653	0.379	10 913 \pm 425

**Figure 3.** Mean magnetic field modulus $\langle B \rangle$ of NGC 1624-2 measured using the split components of the magnetically resolved line C IV $\lambda 5812$ against the rotation phase.**Figure 4.** As Fig. 1, but $\langle B_z \rangle$ measured using the He I 5876 Å and He I 6678 Å lines.

0.03 and 0.35 and do not show rotational modulation. This suggests that they are most likely formed beyond the Alfvén radius.

Our analysis of the observations of NGC 1624-2, in the scenario of an oblique magnetic rotator, indicates that stronger emissions in the hydrogen and helium emission lines are detected when the magnetically confined cooling disc is seen closer to face-on, while the emission contribution is reduced when the cooling disc is seen closer to edge-on (see Fig. 2).

No measurements using the He I emission lines were presented in the study of Wade et al. (2012b). Our $\langle B_z \rangle$ values are predominantly negative and, similar to the measurements of other spectral lines, show clear variability over the rotation period, with the negative $\langle B_z \rangle$ extremum observed around phase 0, where the photospheric absorption lines show a positive $\langle B_z \rangle$ extremum. The distribution of our measurement values over the rotation period obtained using the He I $\lambda 5876$ and $\lambda 6678$ lines, which are the strongest in the $2^3P^0 - n^3D$ and the $2^1P^0 - n^1D$ series, respectively, is presented in Fig. 4. The significant data point dispersion and the presence of two outliers in the measurements of He I $\lambda 5876$ close to the rotation phase 0.2 is caused by the short-term variability of the line intensity on a time-scale of several days, and is likely a consequence of either the pulsational variability recently detected by Kurtz et al. (2020) or a time-variable structure of gas flows within the magnetosphere (ud-Doula et al. 2013).

The origin of the emission in the He I lines in the red spectral region is not well understood. A long time ago, Auer & Mihalas (1972) showed that NLTE effects are quite small for He I lines in the blue-violet region of the spectrum, whereas the red He I lines, in particular He I $\lambda 5876$ and He I $\lambda 6678$, are strongly affected by departures from LTE. A large discrepancy between observations and their NLTE results occurred for He I $\lambda 5876$, where the observed lines are consistently stronger than computed. However, the presented NLTE calculations always remained in absorption. Only at the highest temperatures of about 50 000 K the NLTE results predicted that lines come into emission.

Several mechanisms were suggested since then to understand the appearance of the emission observed in these lines. To explain the emissions in the He I $\lambda 5876$, $\lambda 6678$ lines in the early-type star λ Eri, Smith et al. (1997) suggested that emission can be produced in a dense slab that is optically thick in the Lyman continuum. To produce a large enough column density for an observable feature, the requirement was made that the slab must be cohesive and is confined in a magnetic loop to resist the acceleration of the ambient wind.

The presence of variable Zeeman features corresponding to a longitudinal field of negative polarity observed in the He I emission lines, while high-excitation emission O III lines show the same polarity as the photospheric absorption lines, is puzzling and currently difficult to interpret. One alternative hypothesis could be that the

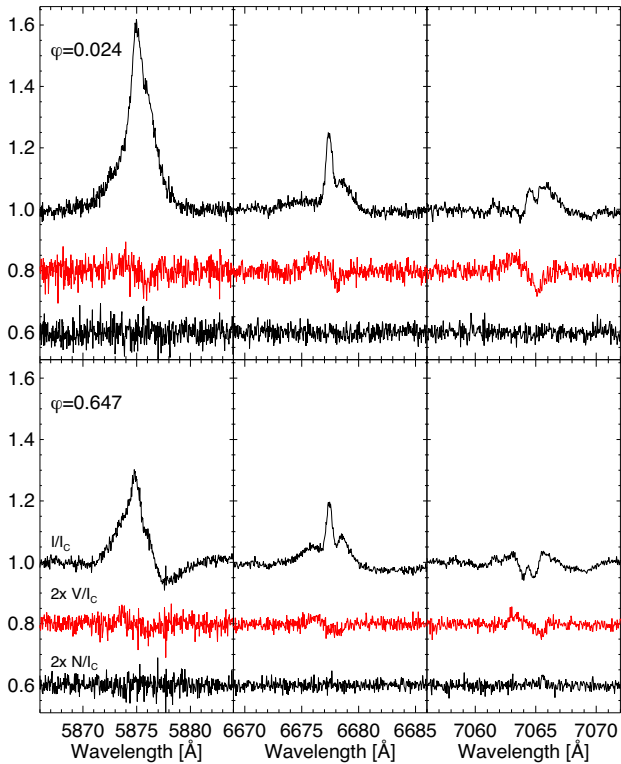


Figure 5. Examples of Stokes I (top), Stokes V (middle, shifted to 0.8 and multiplied by 2), and null (bottom, shifted to 0.6) profiles of the emission lines He I λ 5876, He I λ 6678, and He I λ 7065 at two phases.

He I Stokes I and V profiles have a composite structure and present a contribution of several components. In Fig. 5, we present the Stokes I , V , and null profiles for all three He I emission lines at two rotational phases. Indeed, depending on the line, the observed Stokes I profiles indicate a rather complex variable structure consisting of at least two or three components (see also Figs A4–A6). It is quite possible that there is a correspondence between the different parts of the Stokes I profiles and those of the Stokes V profiles. The resulting composite Stokes V profiles would then present just a blend of the individual Stokes V profiles corresponding to different parts of the Stokes I profiles. It is noteworthy that for the majority of the obtained observations, the shape of the Stokes V profiles displayed in Figs A4–A6 cannot be explained in terms of the Zeeman effect: if these profiles are indeed formed in a hydrostatic stellar atmosphere lacking gradients in velocity and magnetic field as a function of optical depth (e.g. Sanchez Almeida, Collados & del Toro Iniesta 1989; López Ariste 2002), they always have the zero-order moment equal to zero, that is the integral of Stokes V over the region of the spectral line in Stokes I is equal to zero. The observed differences between the areas corresponding to the blue and red parts of the Stokes V profiles calculated for all three He I emission lines are presented in Fig. 6. The differences were calculated only in rotation phases with a lower impact of the noise on the shape of the Stokes V profiles. As this figure shows, for all three lines the differences between the areas corresponding to the blue and red parts of the Stokes V profiles are significant.

The changes in emission strength of the He lines and the different sign of the longitudinal magnetic field in these lines can also be understood within the following scenario. For a dipole magnetic field, the magnetic field lines reverse their orientation at the equator relative

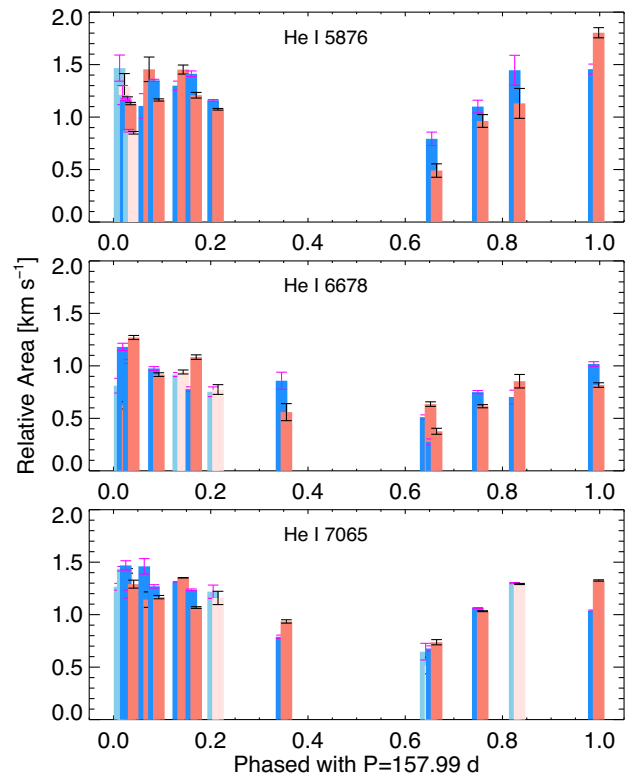


Figure 6. Differences between the relative areas of the blue and red parts of the Stokes V profiles calculated at different rotation phases for the emission lines He I λ 5876, 6678, and 7065. The lighter colour represents the cases where the differences in the areas are within the measurement uncertainties and the darker colour the cases where they are larger than the measurement uncertainties. Error bars for each calculated blue and red part of the Stokes V profiles are presented at the top of the individual bars.

to the pole. If emitting material accumulates in the magnetosphere at the magnetic equator, it experiences a magnetic field of opposite orientation to that at the magnetic pole. Thus, the longitudinal magnetic field measured in the He I lines as seen in emission from the magnetospheric material at the magnetic equator would have a sign opposite from the longitudinal field measured from a photospheric absorption line. The extended region near the equator with an elevated density seems like a plausible source of circumstellar emission (see Fig. 7 for an illustration). The magnetic field there has an opposite orientation to that dominating the upper hemisphere of the photosphere. Then, as the star rotates, the longitudinal component of the magnetic field in the emitting region becomes weaker, and the projected area of the emitting region diminishes, and possibly becomes partially occulted by the star.

Another alternative hypothesis could be related to the complex structure of the magnetospheric circumstellar environment of NGC 1624-2 and the possible presence of a reconnection-driven emission process. To understand the behaviour of the gas flow and the mass distribution within the magnetosphere, we carried out first MHD numerical simulations for this star.

4 MHD NUMERICAL SIMULATIONS

A dipolar magnetic field with a polar field strength of 16 kG will strongly alter the gas flow from the star and inhibit mass loss. The

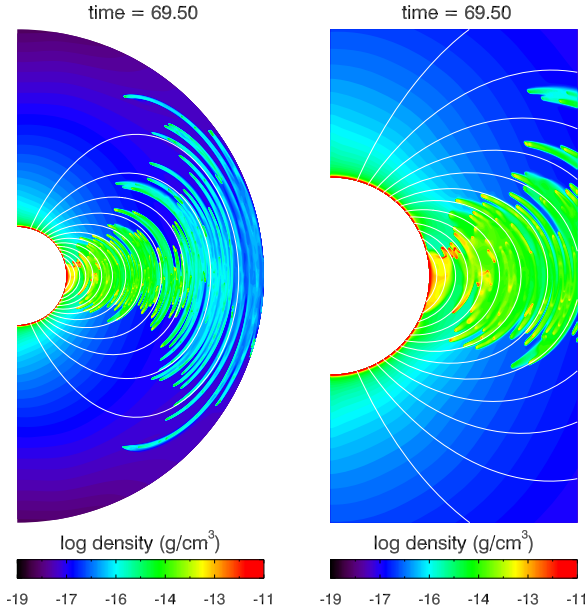


Figure 7. Mass density and magnetic field structure in the vicinity of the star. *Left:* the whole simulation box. *Right:* zoom into the central region. The unit of the time stamps is ks.

impact of the magnetic field is described by the wind confinement parameter, $\eta_* = B_{\text{eq}}^2 R_*^2 / \dot{M} v_\infty$, where B_{eq} is the field strength on the stellar surface at the magnetic equator, R_* the stellar radius, \dot{M} the mass-loss rate with no magnetic field, and v_∞ the terminal velocity of the stellar wind (ud-Doula & Owocki 2002). For NGC 1624-2, $\eta_* = 1.5 \times 10^4$ was found by Wade et al. (2012b), which results in a value of $11.3 R_*$ for the Alfvén radius, which indicates the extent of the magnetically dominated region. Within that region, the magnetic field will keep its dipole geometry and gas flowing from the star at low to mid latitudes will be trapped. Only gas originating from the polar caps leaves the system unimpeded along open field lines.

To study the field geometry, mass distribution, and gas motions in the vicinity of the star, we ran a series of numerical simulations. The general model set-up is described in Küker (2017). We used the NIRVANA MHD code (Ziegler 2008) in spherical polar coordinates. The geometry is axisymmetric with respect to the polar axis of the magnetic field and the gas is assumed isothermal, with the gas temperature being the effective temperature of the star. No rotation is included. As the model does not include cooling, magnetic diffusion has been added with a diffusion coefficient of $10^{15} \text{ cm}^2 \text{ s}^{-1}$. The stellar and wind parameters have been adopted from Wade et al. (2012b). We thus use a stellar mass of 34 solar masses, a stellar radius of 10 solar radii and an effective temperature of 35 000 K. The mass-loss rate is $1.6 \times 10^{-7} M_\odot \text{ yr}^{-1}$ and the terminal wind velocity is 2785 km s^{-1} . The start solution is a dipole magnetic field and a velocity law given by

$$v(r) = v_\infty \left(1 - \frac{R_*}{r} \right). \quad (2)$$

The initial mass distribution is determined by the velocity law (2) and the mass-loss rate, i.e.

$$\rho = \frac{\dot{M}}{4\pi v r^2}. \quad (3)$$

A radiative force term after Castor, Abbott & Klein (1975) with $\bar{Q} = 550$ and $\alpha = 0.55$ is used to drive the wind. The parameters

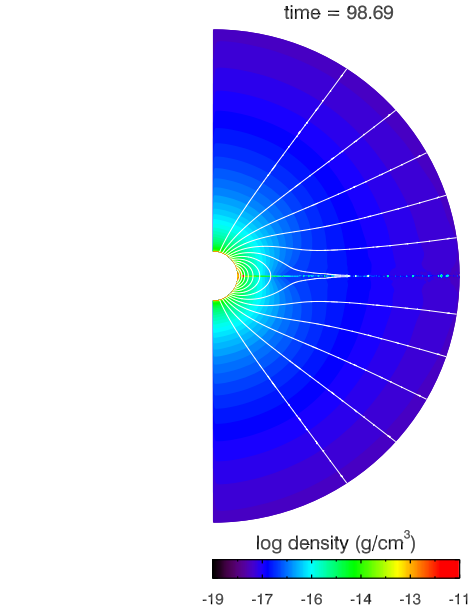


Figure 8. Mass density and magnetic field from a simulation with $B_0 = 1 \text{ kG}$.

have been chosen such that without the magnetic field a stationary solution with the correct wind parameters is produced. We then repeat the computation with a dipole field included. To limit the cost in CPU time, the outer boundary of the simulation box is placed at five stellar radii and a polar field strength of 4 kG is chosen. While this is smaller than the observed field strength of 16 kG, it still leads to an extended region of magnetic confinement with $\eta_* \approx 700$ and an Alfvén radius of 5.4 stellar radii. Within the simulation box, the magnetic field geometry stays close to the original dipolar geometry and only a fraction of the gas flowing from the stellar surface can escape the system. The mass loss rate found by Wade et al. (2012b) is based on a prescription by Vink, de Koter & Lamers (2001) that does not take the magnetic field into account. It therefore refers to the amount of gas that would leave the system if there was no magnetic field.

In the initial phase of the simulation run, the gas flow and mass density undergo drastic changes. While the gas density at high latitude drops, gas piles up in the equatorial plane, where a thin disc forms from which filaments grow that are aligned with the magnetic field. Fig. 7 shows a snapshot of the mass density taken at a time when the system has reached a semistationary state in so far as the general mass distribution with a high-mass concentration at low to mid latitudes does not evolve much anymore. The shape and length of the individual filaments is highly variable, though, and the system does not reach a truly stationary state. Note that all the field lines shown are closed. Compared to the original dipole, the field is slightly compressed by the gas load but the general field topology is unchanged. This is generally different for weak surface fields or at greater distances from the star, where the field lines are stretched away from the star and a thin disc of outflowing material forms.

Fig. 8 shows a snapshot from a simulation with a weaker field of 1 kG. The magnetosphere is much less extended both in radius and latitude and far away from the star the magnetic field is stretched out into a configuration resembling a split monopole with a current sheet in the equatorial plane. The gas forms a thin disc of enhanced mass density in the equatorial plane. The disc is fragmented and the magnetic field is frozen into the fragments. In the equatorial plane the magnetic field forms an elongated tail. At the tip, reconnection

occurs and magnetic flux is carried away by the disc material. We expect a similar picture in case of stronger fields, but at distances from the star outside our current simulation box. Note also that for the stronger magnetic field in Fig. 7, the regions of the stellar surface where open field lines originate is limited to a small range of latitudes around the poles. We expect this effect to be even stronger with a dipole field strength as large as 20 kG. The right-hand panel of Fig. 7 shows a zoom-in to the inner part of the simulation box.

At the time shown, the magnetosphere is still forming and the filaments become longer. Close to the star the mass distribution is quite complex, with an increased mass density at low latitudes close to the stellar surface and blobs of gas at low to mid latitudes. Within the filament structure, gas moves back and forth along the field lines and inward towards the star. The mass distribution is distinctly asymmetric with respect to the equatorial plane. At this point we cannot predict the final structure and extent of the magnetosphere but we notice the high-mass density at low to mid latitudes. To summarize, while there must be strong currents present to exert a Lorentz force strong enough to trap the gas, we do not find any changes of the field topology close to the star that would hint at possible reconnection events in that region.

5 DISCUSSION

Slow rotators with strong magnetic fields, such as NGC 1624-2, form dynamical magnetospheres, in which material flows along closed magnetic field loops from both magnetic poles, colliding near the magnetic equator and then falling back on to the stellar surface, leading to complex flows in the magnetosphere. NGC 1624-2's magnetosphere was estimated to extend to an Alfvén radius R_A of more than eleven stellar radii, hence trapping 95 per cent of the outflowing wind, much more than other magnetic O stars that have an R_A of just a few stellar radii (David-Uraz et al. 2019). A much larger and denser magnetosphere compared to that of any other magnetic O-type star was also confirmed by *Chandra* observations, where the high X-ray luminosity, its variation with stellar rotation, and its large attenuation are consistent with a large dynamical magnetosphere with magnetically confined wind shocks (Petit et al. 2015).

NGC 1624-2 is the only magnetic O-type star for which the variability of both the longitudinal magnetic field and the mean magnetic field modulus is currently studied. The approximately sinusoidal variation of $\langle B_z \rangle$ and the ratio of the values of the extrema of $\langle B \rangle$ indicate that there is an important component of the field that is dipolar. The absence of a sign reversal of the mean longitudinal field over the rotation cycle indicates that only one magnetic pole is visible over the rotation cycle. Involving the mean field modulus measurements, we find that the geometrical structure of the magnetic field of NGC 1624-2 must depart from a centred dipole. A similar conclusion has been independently obtained by David-Uraz et al. (2021). Notably, among the eleven magnetic O-type stars with known $\langle B_z \rangle$ variation curves, for seven stars, HD 108, HD 37022 ($=\theta^1$ Ori C), HD 54879, HD 148937, HD 191612, Tr 16-22, and NGC 1624-2, only one magnetic pole is visible throughout the rotation cycle (Donati et al. 2006; Petit et al. 2008; Wade et al. 2012a; Naze et al. 2016, this work; Shultz & Wade 2017; Hubrig et al. 2020). This implies that, due to an unfavourable inclination of the rotation axis, a larger fraction of their surfaces can never be observed, leaving the structure of the field over the invisible surface only constrained by the assumption of a tilted centred dipole. There will thus always be a considerable degree of ambiguity left in the magnetic models of these stars.

Our $\langle B_z \rangle$ values measured using He I emission lines are predominantly negative and, similar to the measurements of other spectral lines, show clear variability over the rotation period, with the negative $\langle B_z \rangle$ extremum observed around phase 0, where the photospheric absorption lines show a positive $\langle B_z \rangle$ extremum. To explain the presence of variable Stokes V signatures corresponding to a longitudinal field of negative polarity in these lines, we suggest three alternative scenarios: one is related to a composite structure representing the contribution of several components, another one referring to the complex structure of the magnetospheric circumstellar environment of NGC 1624-2 with the possible presence of a reconnection-driven emission process, and a third one where the He I emission comes from circumstellar material accumulated in the equatorial region of the magnetosphere, where the dipolar magnetic field shows an inverted sign with respect to the pole.

As of today, magnetic reconnection is best studied in the solar photosphere, but it is not clear how the scenarios developed for the Sun can apply for massive stars. Although the detection of a negative longitudinal field inferred from the He I emission lines was reported about 8 yr ago, neither magnetohydrodynamical (MHD) simulations nor analytical models have been developed to provide a description of the magnetospheric structure permitting the reproduction of the observed phenomenon. According to Owocki et al. (2016) the presence of a huge magnetosphere and a very strong surface field are prohibitively expensive to model using numerical MHD. Our MHD numerical simulations show that while reconnection events indeed occur in magnetospheres of massive stars and the magnetic flux is carried away by the disc material, such events take place too far from the stellar surface where He I emission lines are formed.

On the other hand, as the shape of the Stokes V profiles of the He I emission lines displayed in Figs A4–A6 cannot be explained in terms of the Zeeman effect, the alternative hypothesis related to a composite structure of Stokes I and V profiles presenting the contribution of several components appears currently more promising. It is possible that future observations of all four Stokes parameters in these lines will help to disentangle the contribution of different line components.

ACKNOWLEDGEMENTS

We would like to thank the anonymous referee for their rigid review of our article, especially for their suggestions concerning the interpretation of the inverted magnetic field in the helium lines. We also thank G. Mathys for a discussion on the field modulus. SPJ is supported by the German Leibniz-Gemeinschaft, project number P67-2018. Based on observations collected at the Canada–France–Hawaii Telescope (CFHT), which is operated by the National Research Council of Canada, the Institut National des Sciences de l'Univers of the Centre National de la Recherche Scientifique of France, and the University of Hawaii. Also based on archival observations obtained at the Bernard Lyot Telescope (Pic du Midi, France) of the Midi-Pyrénées Observatory, which is operated by the Institut National des Sciences de l'Univers of the Centre National de la Recherche Scientifique of France. Based on data acquired with the Potsdam Echelle Polarimetric and Spectroscopic Instrument (PEPSI) using the Large Binocular Telescope (LBT) in Arizona. This work has made use of the VALD, operated at Uppsala University, the Institute of Astronomy RAS in Moscow, and the University of Vienna.

DATA AVAILABILITY

The ESPaDO nS data underlying this article are available in the CFHT Science Archive at <https://www.cadc-ccda.hia-ihp.nrc->

cnrc.gc.ca/en/cfht/ and can be accessed with the object name. Similarly, the Narval data as well as the ESPaDOnS are available in PolarBase at <http://polarbase.irap.omp.eu>. The PEPSI and ARCÉS data underlying this article will be shared on a reasonable request to the corresponding author.

REFERENCES

- Auer L. H., Mihalas D., 1972, *ApJS*, 24, 193
 Castor J. I., Abbott D. C., Klein R. I., 1975, *ApJ*, 195, 157
 Claret A., Bloemen S., 2011, *A&A*, 529, A75
 Corcoran M., Ray T. P., 1997, *A&A*, 321, 189
 David-Uraz A. et al., 2019, *MNRAS*, 483, 2814
 David-Uraz A., Petit V., Shultz M. E., Fullerton A. W., Erba C., Keszthelyi Z., Seadrow S., Wade G. A., 2021, *MNRAS*, 501, 2677
 Donati J.-F., Semel M., Rees D. E., 1992, *A&A*, 265, 669
 Donati J.-F., Semel M., Carter B. D., Rees D. E., Collier Cameron A., 1997, *MNRAS*, 291, 658
 Donati J.-F., Babel J., Harries T. J., Howarth I. D., Petit P., Semel M., 2002, *MNRAS*, 333, 55
 Donati J.-F., Howarth I. D., Bouret J.-C., Petit P., Catala C., Landstreet J., 2006, *MNRAS*, 365, 6
 Finkenzeller U., 1985, *A&A*, 151, 340
 Grunhut J. H. et al., 2009, *MNRAS*, L400, 94
 Grunhut J. H. et al., 2017, *MNRAS*, 465, 2432
 Howarth I. D. et al., 2007, *MNRAS*, 381, 433
 Hubrig S., Nesvacil N., 2007, *MNRAS*, 378, L16
 Hubrig S., Järvinen S. P., Schöller M., Hummel C. A., 2020, *MNRAS*, 491, 281
 Küker M., 2017, *Astron. Nachrichten*, 338, 868
 Kupka F., Dubernet M.-L., VAMDC Collaboration, 2011, *Balt. Astron.*, 20, 503
 Kurtz D. W., Hubrig S., Järvinen S. P., Schöller M., 2020, *Res. Notes Am. Astron. Soc.*, 4, 157
 López Ariste A., 2002, *ApJ*, 564, 379
 Mathys G., 1989, *Fundam. Cosm. Phys.*, 13, 143
 Muzerolle J., D'Alessio P., Calvet N., Hartmann L., 2004, *ApJ*, 617, 406
 Nazé Y., Barbá R., Bagnulo S., Morrell N., Gamen R., 2016, *A&A*, 596, A44
 Owocki S. P., ud-Doula A., Sundqvist J. O., Petit V., Cohen D. H., 2016, *MNRAS*, 462, 3830
 Petit V., Wade G. A., Drissen L., Montmerle T., Alecian E., 2008, *MNRAS*, 387, L23
 Petit V. et al., 2013, *MNRAS*, 429, 398
 Petit P., Louge T., Théado S., Paletou F., Manset N., Morin J., Marsden S. C., Jeffers S. V., 2014, *PASP*, 126, 469
 Petit V. et al., 2015, *MNRAS*, 453, 3288
 Preston G. W., 1967, *ApJ*, 150, 547
 Ricker G. R. et al., 2014, in Oschmann J. M. Jr, Clampin M., Fazio G. G., MacEwen H. A., eds, *Proc. SPIE Conf. Ser. Vol. 9143, Space Telescopes and Instrumentation 2014: Optical, Infrared, and Millimeter Wave*. SPIE, Bellingham, p. 914320
 Ryabchikova T., Piskunov N., Kurucz R. L., Stempels H. C., Heiter U., Pakhomov Y., Barklem P. S., 2015, *Phys. Scr.*, 90, 054005
 Sanchez Almeida J., Collados M., del Toro Iniesta J. C., 1989, *A&A*, 222, 311
 Schöller M. et al., 2017, *A&A*, 599, A66
 Shultz M., Wade G. A., 2017, *MNRAS*, 468, 3985
 Smith M. A., Cohen D. H., Hubeny I., Plett K., Basri G., Johns-Krull C. M., MacFarlane J. J., Hirata R., 1997, *ApJ*, 481, 467
 Stibbs D. W. N., 1950, *MNRAS*, 110, 395
 Strassmeier K. G. et al., 2015, *Astron. Nachr.*, 336, 324
 Strassmeier K. G. et al., 2018, in Evans J. C., Simard L., Takami H., eds, *Proc. SPIE Conf. Ser. Vol. 10702, Ground-based and Airborne Instrumentation for Astronomy VII*. SPIE, Bellingham, p. 1070212
 ud-Doula A., Owocki S. P., 2002, *ApJ*, 576, 413
 ud-Doula A., Sundqvist J. O., Owocki S. P., Petit V., Townsend R. H. D., 2013, *MNRAS*, 428, 2723
 Vink J. S., de Koter A., Lamers H. J. G. L. M., 2001, *A&A*, 369, 574
 Wade G. A. et al., 2012a, *MNRAS*, 419, 2459
 Wade G. A. et al., 2012b, *MNRAS*, 425, 1278
 Walborn N. R., 1972, *AJ*, 77, 312
 Wang et al., 2003, *Proceedings of the SPIE*, 4841, 1145
 Ziegler U., 2008, *Comput. Phys. Commun.*, 179, 227

APPENDIX A: PROFILES FOR LONGITUDINAL MAGNETIC FIELD MEASUREMENTS

LSD Stokes I , V , and null profiles are presented in Fig. A1 for the line list with absorption lines, in Fig. A2 for the same line list, but without the Si absorption lines, in Fig. A3 for the high-excitation O III $\lambda 7455$ emission line, in Fig. A4 for the He I $\lambda 5876$ emission line, in Fig. A5 for the He I $\lambda 6678$ emission line, and in Fig. A6 for the He I $\lambda 7065$ emission line. The plots are sorted by rotational phase. Shaded regions in Stokes V and null panels indicate the mean uncertainty.

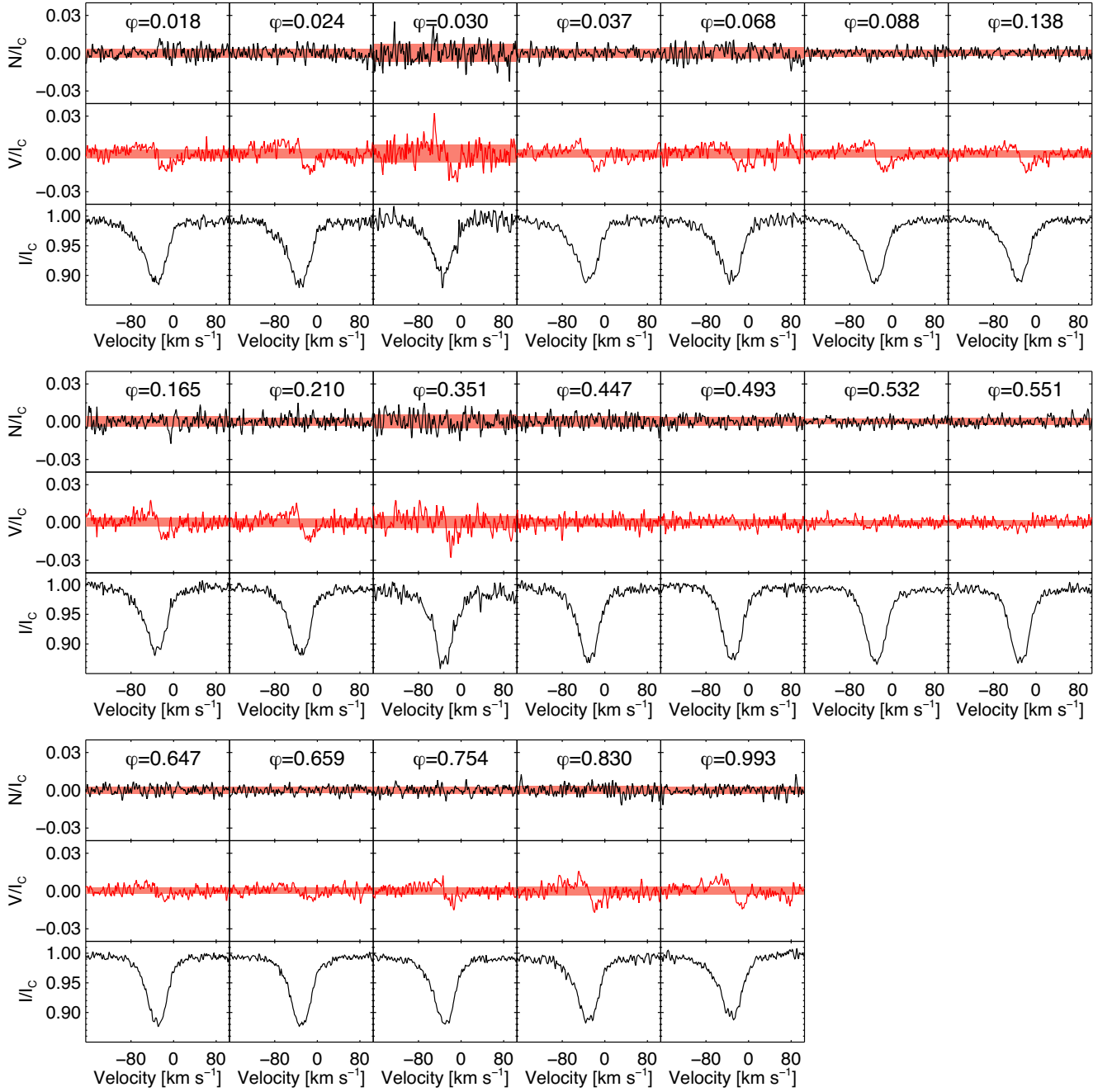


Figure A1. LSD Stokes I , V , and null profiles for the line list with absorption lines. The plots are sorted by rotational phase. Shaded regions in Stokes V and null panels indicate the mean uncertainty.

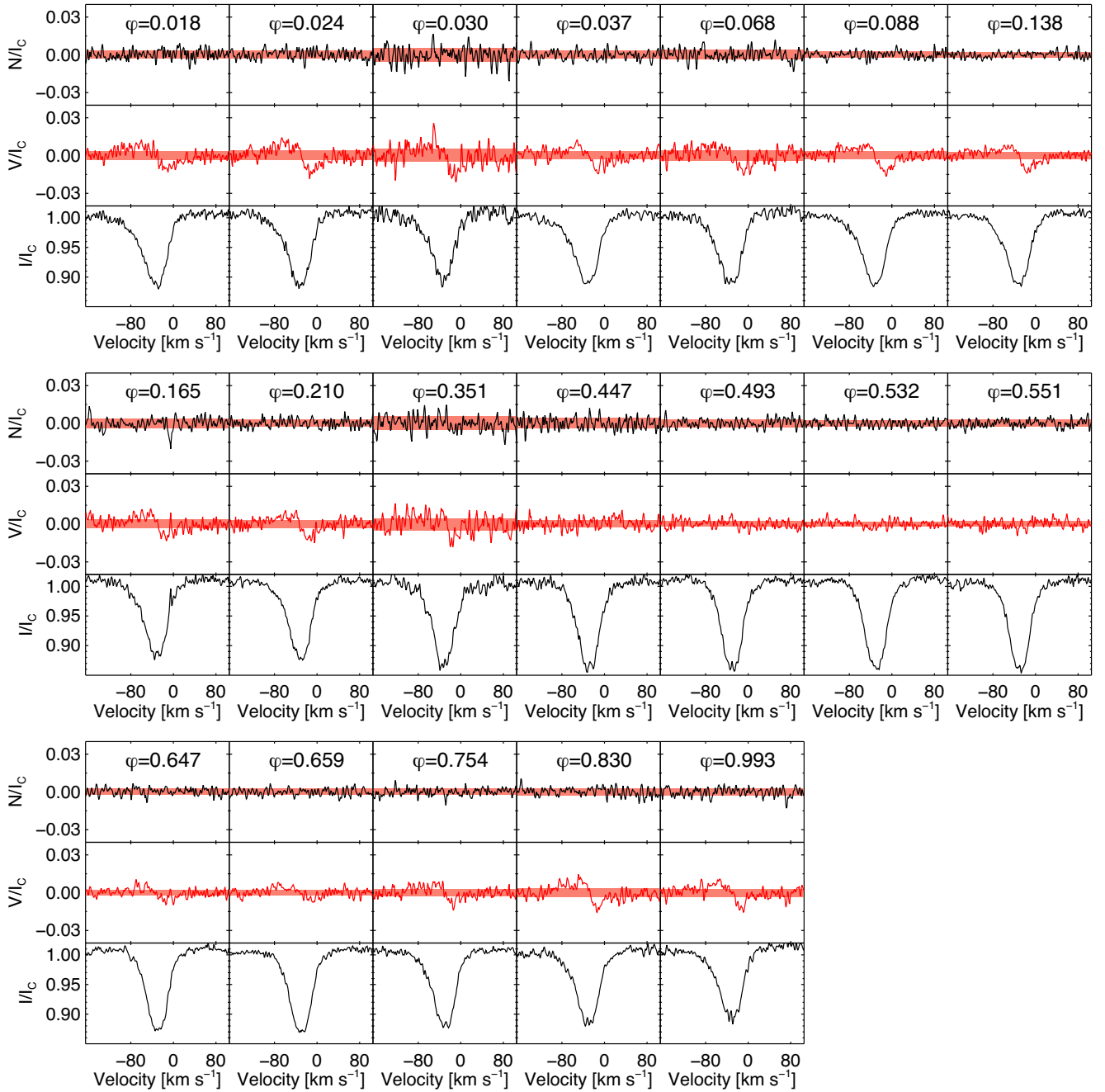


Figure A2. As Fig. A1, but for the line list without Si absorption lines.

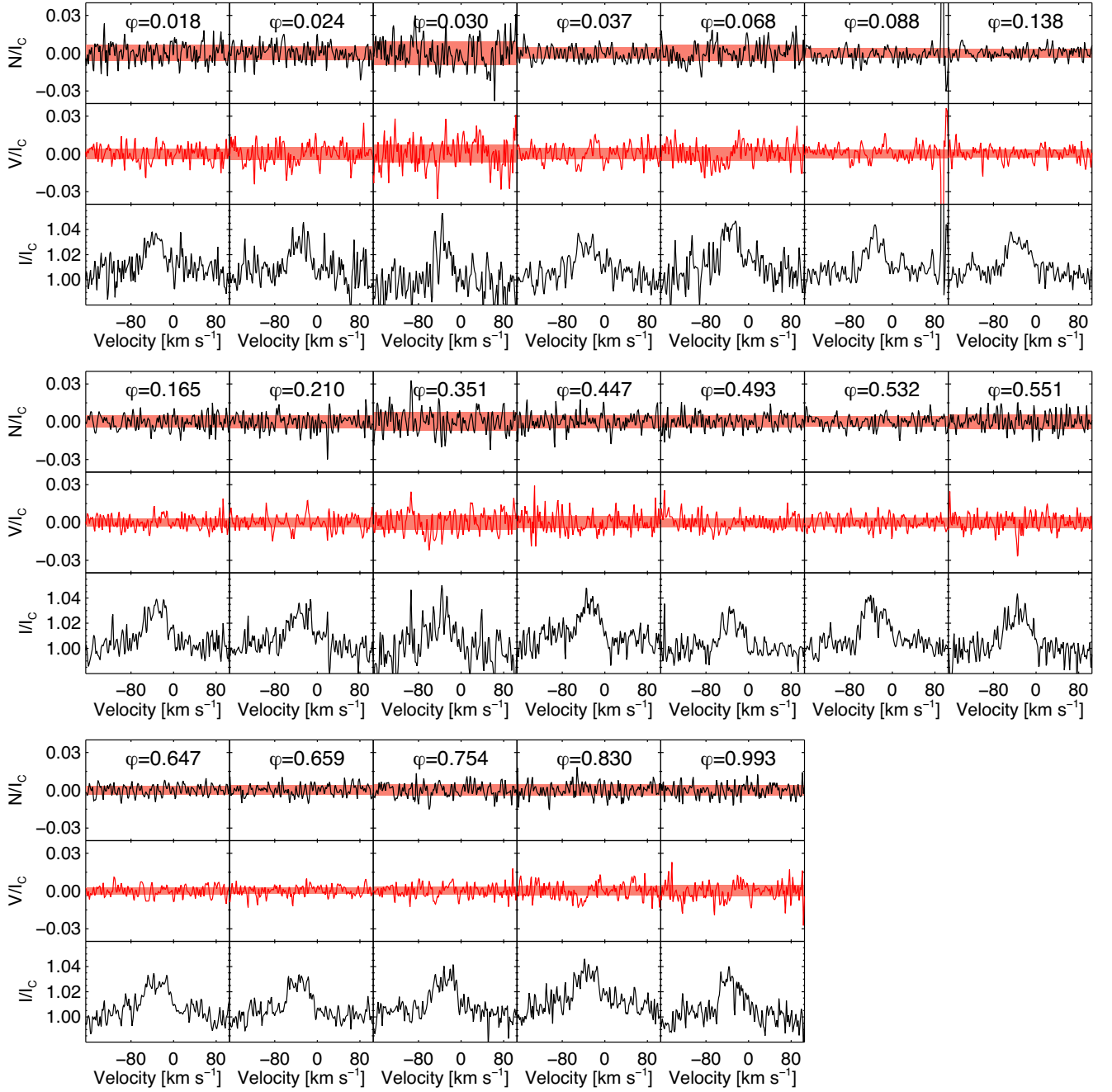


Figure A3. Stokes I , V , and null profiles in velocity frame for the high-excitation O III $\lambda 7455$ emission line (see Fig. A1).

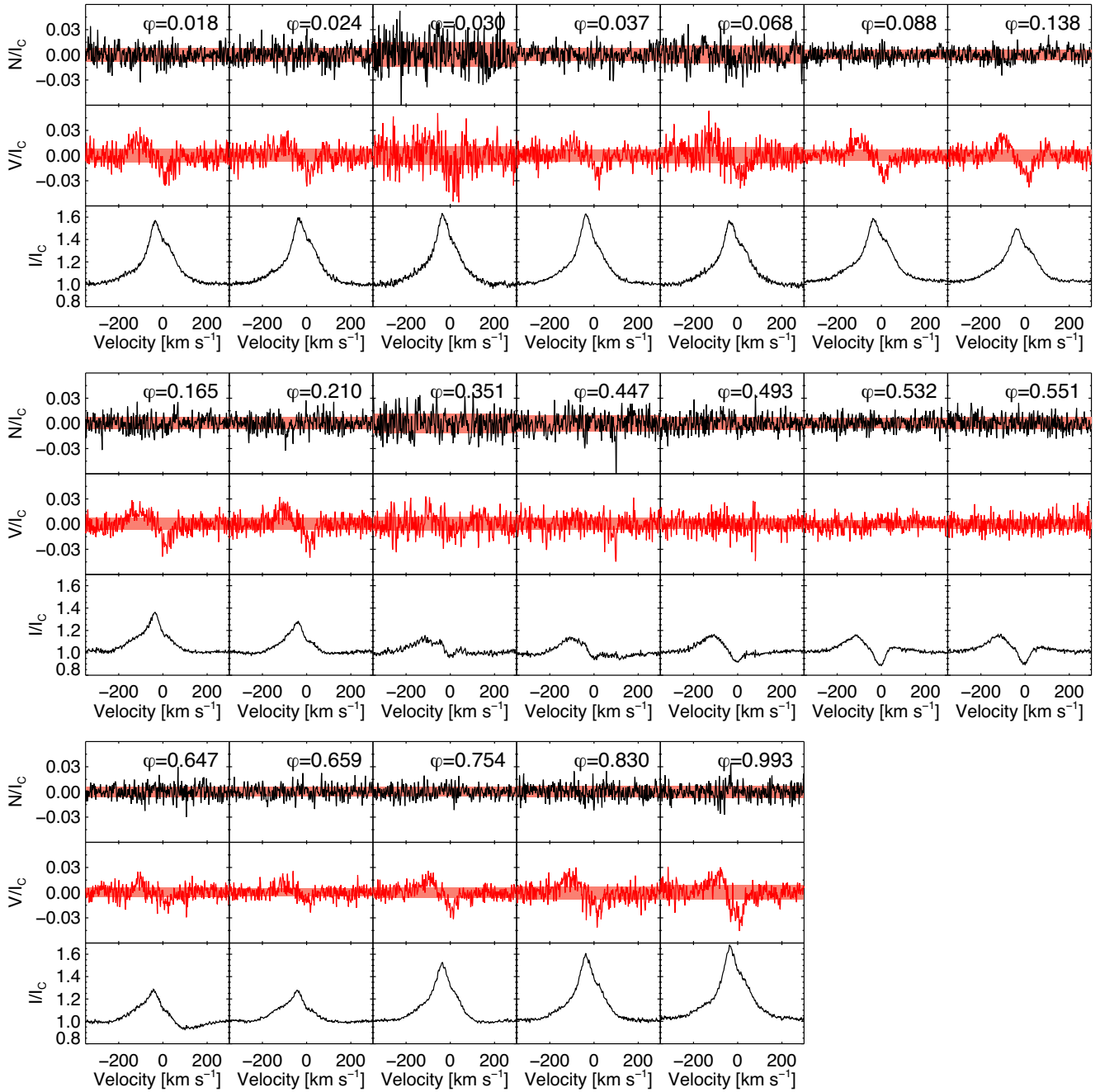


Figure A4. As Fig. A3, but for the He I $\lambda 5876$ emission line.

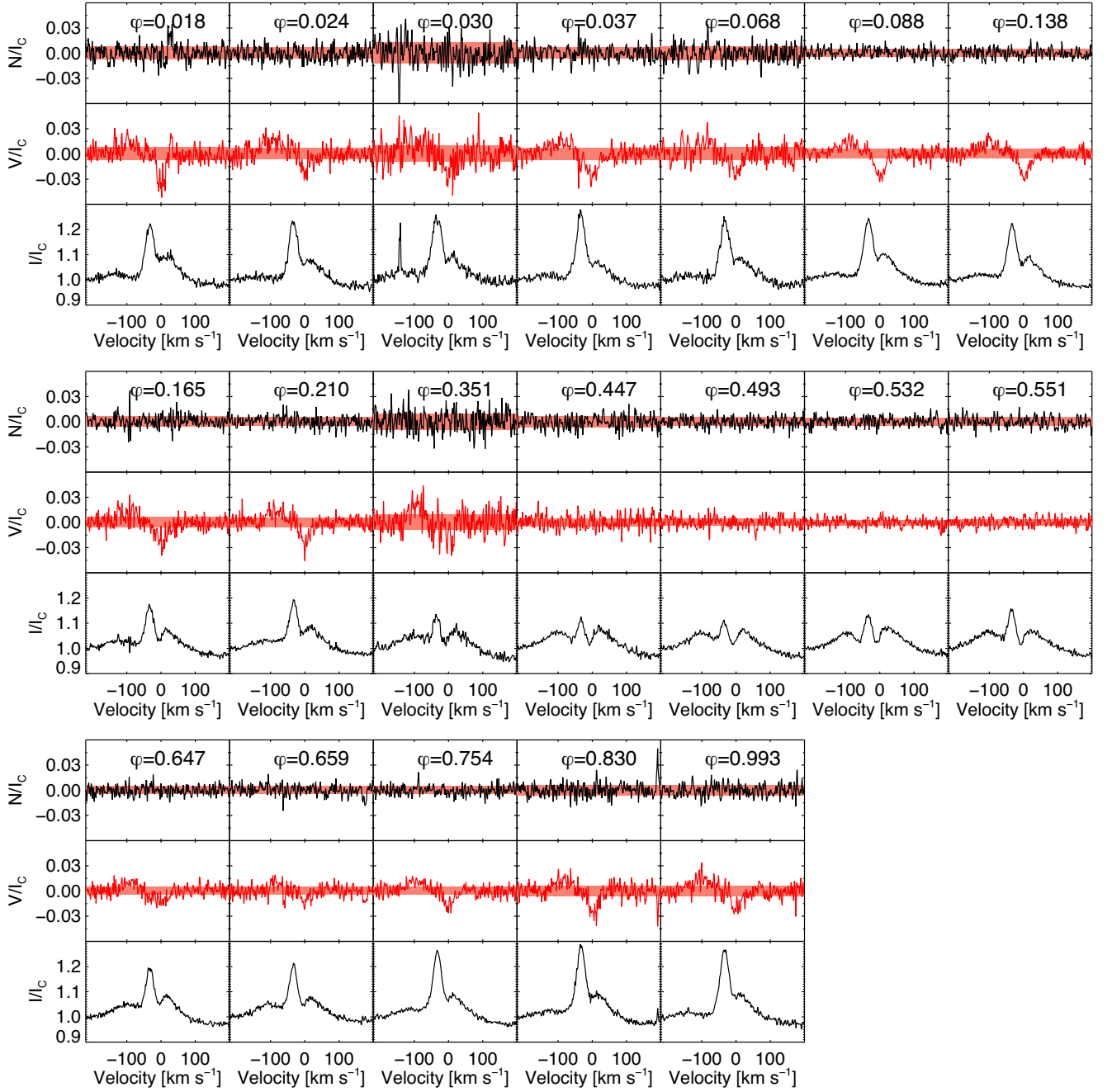


Figure A5. As Fig. A3, but for the He I $\lambda 6678$ emission line.

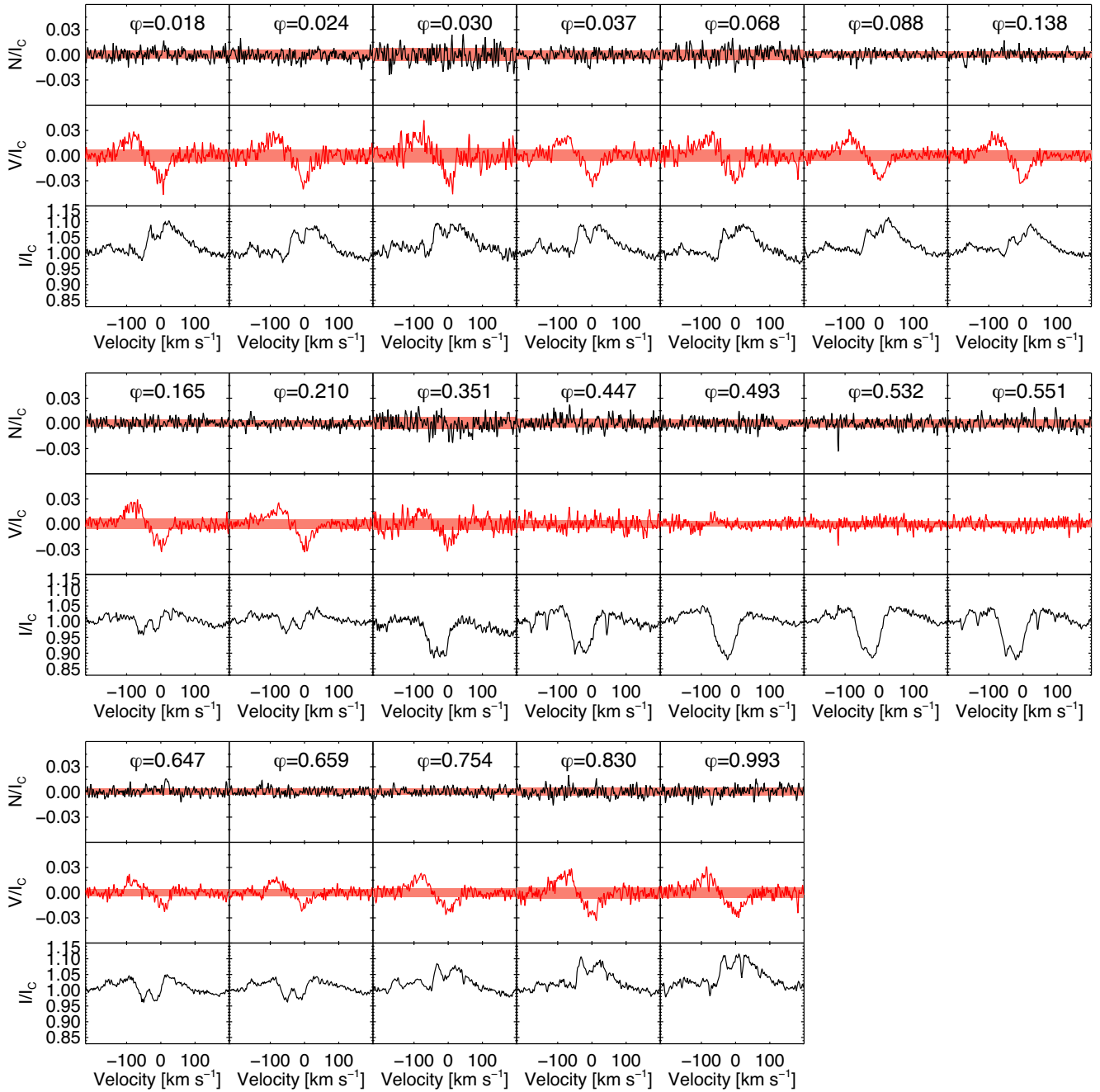


Figure A6. As Fig. A3, but for the He I $\lambda 7065$ emission line.

APPENDIX B: NEBULAR LINES

The strength of the forbidden [O I] nebular lines at $\lambda 6300$ and $\lambda 6363$ as a function of rotation phase is displayed in Fig. B1.

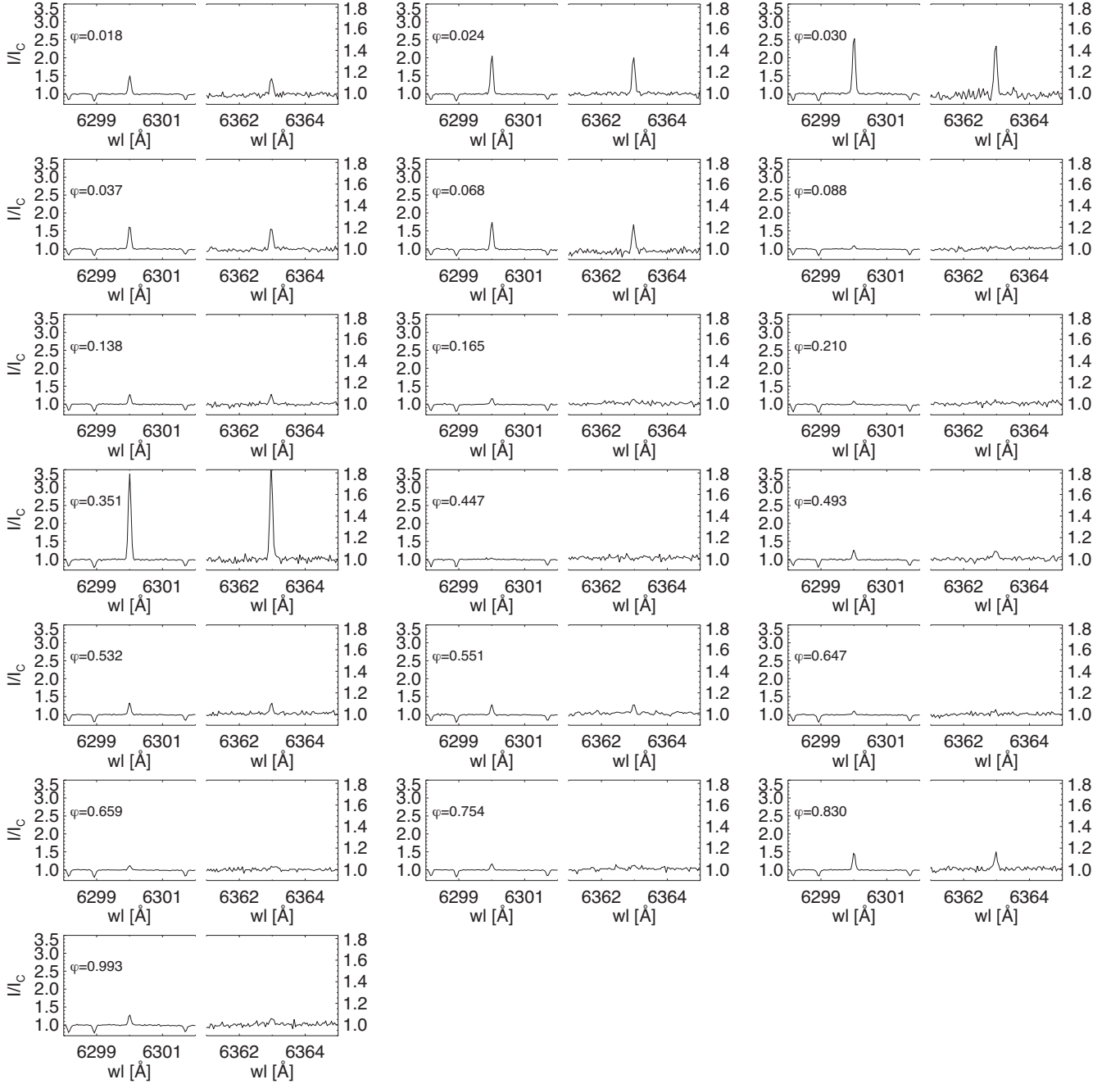


Figure B1. The strength of the forbidden [O I] nebular lines at $\lambda 6300$ (left) and $\lambda 6363$ (right) as a function of rotation phase.

This paper has been typeset from a \LaTeX file prepared by the author.